**Acknowledgements** We thank the Fundação de Amparo a Pesquisa do Estado de São Paulo (FAPESP) for financial support, the CECAV/IBAMA for authorizing cave samples collection and the GEEP-Açungui Speleological Group and E. Barni for supporting field work.

**Competing interests statement** The authors declare that they have no competing financial interests.

**Correspondence** and requests for materials should be addressed to F.W.C. Jr (fdacruz@geo.umass.edu).

# Water-rich basalts at mid-ocean-ridge cold spots

**Marco Ligi[1], Enrico Bonatti[1,2,3], Anna Cipriani[1,2] & Luisa Ottolini[4]**

[1]*Istituto Scienze Marine, Geologia Marina, CNR, Via Gobetti 101, 40129 Bologna, Italy*
[2]*Lamont Doherty Earth Observatory, Columbia University, Palisades, New York 10964, USA*
[3]*Dipartimento di Scienze della Terra, Università "La Sapienza", Piazzale Aldo Moro 5, 00187 Rome, Italy*
[4]*Istituto di Geoscienze e Georisorse, Sezione di Pavia, CNR, Via Ferrata 1, 27100 Pavia, Italy*

**Although water is only present in trace amounts in the sub-oceanic upper mantle, it is thought to play a significant role in affecting mantle viscosity, melting and the generation of crust at mid-ocean ridges. The concentration of water in oceanic basalts[1,2] has been observed to stay below 0.2 wt%, except for water-rich basalts sampled near hotspots and generated by 'wet' mantle plumes[3–5]. Here, however, we report unusually high water content in basaltic glasses from a cold region of the mid-ocean-ridge system in the equatorial Atlantic Ocean. These basalts are sodium-rich, having been generated by low degrees of melting of the mantle, and contain unusually high ratios of light versus heavy rare-earth elements, implying the presence of garnet in the melting region. We infer that water-rich basalts from such regions of thermal minima derive from low degrees of 'wet' melting greater than 60 km deep in the mantle, with minor dilution by melts produced by shallower 'dry' melting—a view supported by numerical modelling. We therefore conclude that oceanic basalts are water-rich not only near hotspots, but also at 'cold spots'.**

The water content of the oceanic upper mantle can be estimated from the water concentration in mid-ocean-ridge basalt (MORB) glasses, after correcting for the effects of degassing and magmatic differentiation. The $H_2O$ content of normal MORB (N-MORB) is generally below 0.2 wt% (ref. 1). Given that $H_2O$ is about as incompatible as Ce, and assuming ~10% average degree of melting of the mantle upwelling below mid-ocean ridges (MORs), the mantle source of N-MORB is assumed to contain 0.01–0.02 wt% $H_2O$ (ref. 2). However, basalts from topographically swollen portions of MORs have $H_2O$ concentrations higher than those of N-MORB (Fig. 1). These swollen ridges are generally interpreted as being influenced by hot plumes rising from the transition zone or from even deeper in the mantle. Thus, the $H_2O$ content of the mantle source of plume-type oceanic basalts is probably significantly higher than that of the N-MORB source region. For example, the mantle source of the Icelandic[3] and Azores platform[4] crust contains between 620 and 920 p.p.m. $H_2O$, that is, several times higher than that of the N-MORB source. Concerning off-ridge hotspots, an $H_2O$ content of 405 ± 190 p.p.m. has been estimated for the mantle source of Hawaiian basalts[5], supporting the hypothesis that plume-type mantle is $H_2O$-rich relative to the N-MORB mantle source. High water and volatile contents lower the mantle solidus, so that the mantle melts deeper and to a higher degree during its ascent below MORs.

We report here that the $H_2O$ content of basaltic glasses from the equatorial Mid-Atlantic Ridge (MAR) is significantly higher than that of N-MORB. However, these $H_2O$-rich basalts are associated not with a 'hot' portion of MOR, but with the opposite—that is, a thermal minimum in the ridge system. We will discuss a model that

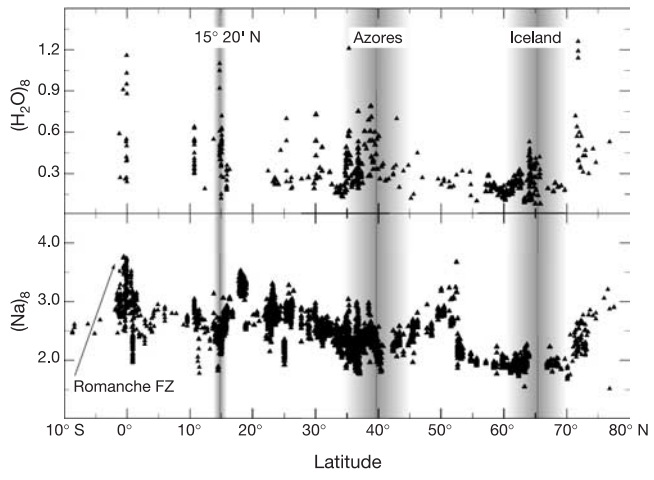


**Figure 1** Distribution of $Na_8$ and $(H_2O)_8$ in MORB glasses along the axis of the Mid-Atlantic Ridge from Iceland to the Equator. Data are from the Supplementary Table, our unpublished results and the Petrological Database of the Ocean Floor (PETDB) of Lamont Doherty Earth Observatory. FZ, fracture zone.

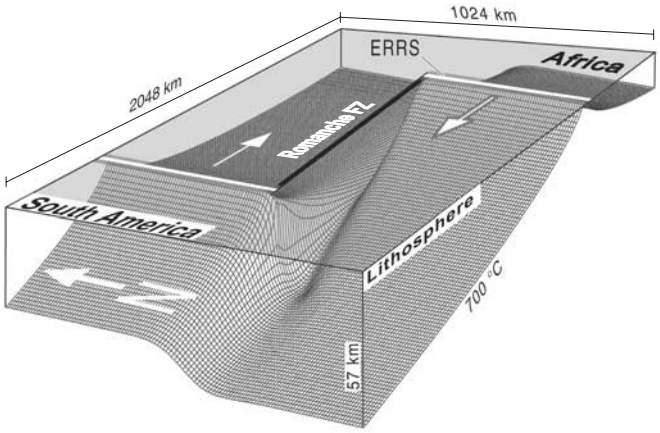


**Figure 2** Geometry of the passive-flow model. The bases of the rigid plates represent the upper boundary layer in our plate-thickening passive mantle flow model. The model shown was obtained by iteratively solving the mantle temperature field at each time step, starting from a constant-thickness plate-flow model. The computed thickness of the African plate lithosphere at the ERRS transform intersection is ~50 km. Mantle flow velocities were estimated by solving a steady-state corner flow in a computational frame 2,048 × 1,024 km wide and 150 km deep (using a grid with 2 × 2 km spacing for each 1 km depth increment), assuming an incompressible homogeneous and isoviscous mantle. Mantle temperatures were predicted by solving the steady-state advection-diffusion equation, using an over-relaxation upwind finite difference method with variable grid spacing (512 × 256 × 101), and highest grid resolution (1 km) at the plate boundaries[28]. Temperature solutions were found assuming 0 °C at the sea floor and 1,330 °C at 150 km depth, assuming the presence of an equatorial MAR cold spot[11,12].

explains why the $H_2O$ content of oceanic basalt is high not only at hotspots, but also at 'cold spots'.

Basaltic glasses were sampled by dredging at several sites along the ~220-km-long MAR segment (the eastern Romanche ridge segment, ERRS) that extends south of the 900-km Romanche transform (Figs 2 and 3). Glasses were selected for freshness, and analysed by ion probe for rare-earth elements (REEs) and $H_2O$, and by electron microprobe for major elements (see Methods). The $H_2O$ content of our glasses ranges from 0.25 to 1.10 wt% (see Supplementary Table). Their depth of eruption is >2,100 m below sea level; thus, they must be undersaturated in $H_2O$ at these depths[6] with little or no $H_2O$ loss during eruption. The absence of vesicles in the glasses supports this conclusion. Their Cl content is <0.11% and mostly below the limit of detection (0.04%), suggesting no contamination by sea water. In order to correct for the effects of differentiation, we calculated $(H_2O)_8$—that is, $H_2O$ normalized to 8 wt% MgO (refs 7, 8)—assuming olivine-plagioclase-clinopyroxene fractionation. The correction lowers somewhat the $H_2O$ values but does not affect relative trends (see Supplementary Table).

$(H_2O)_8$ and $Na_8$ plotted versus latitude along the MAR axis (Fig. 1) reveal variations of basalt water content, with maxima in regions where the MAR is affected by mantle plumes, such as at 62°–70° N (Iceland), 35°–45°N (Azores) and 15° 20′ N. Maxima in $H_2O$ content are generally mirrored by minima in $Na_8$ (Fig. 1), consistent with the idea whereby plume-related high degree of melting and water-rich plume mantle source go together[9,10]. Glasses from the equatorial MAR are an exception to this pattern, in so far as they are $H_2O$-rich while $Na_8$ is also high. High-$Na_8$ basalts are consistent with a low degree of melting in this region[11,12]. Peridotite mineral composition also suggests that the mantle in the equatorial MAR underwent exceptionally low (<5%) degrees of melting[13], probably owing to the combined effects of a regional equatorial Atlantic thermal minimum[11,12], and a strong 'transform cold-edge effect'[14], which cools the ridge as it approaches old/thick/cold lithosphere across transform offsets.

We carried out numerical experiments to estimate the extent to which the upper mantle is cooled by a long-offset, low-slip transform, such as the Romanche, and how partial melting and $H_2O$ distribution are affected. We assumed a 900-km-long transform

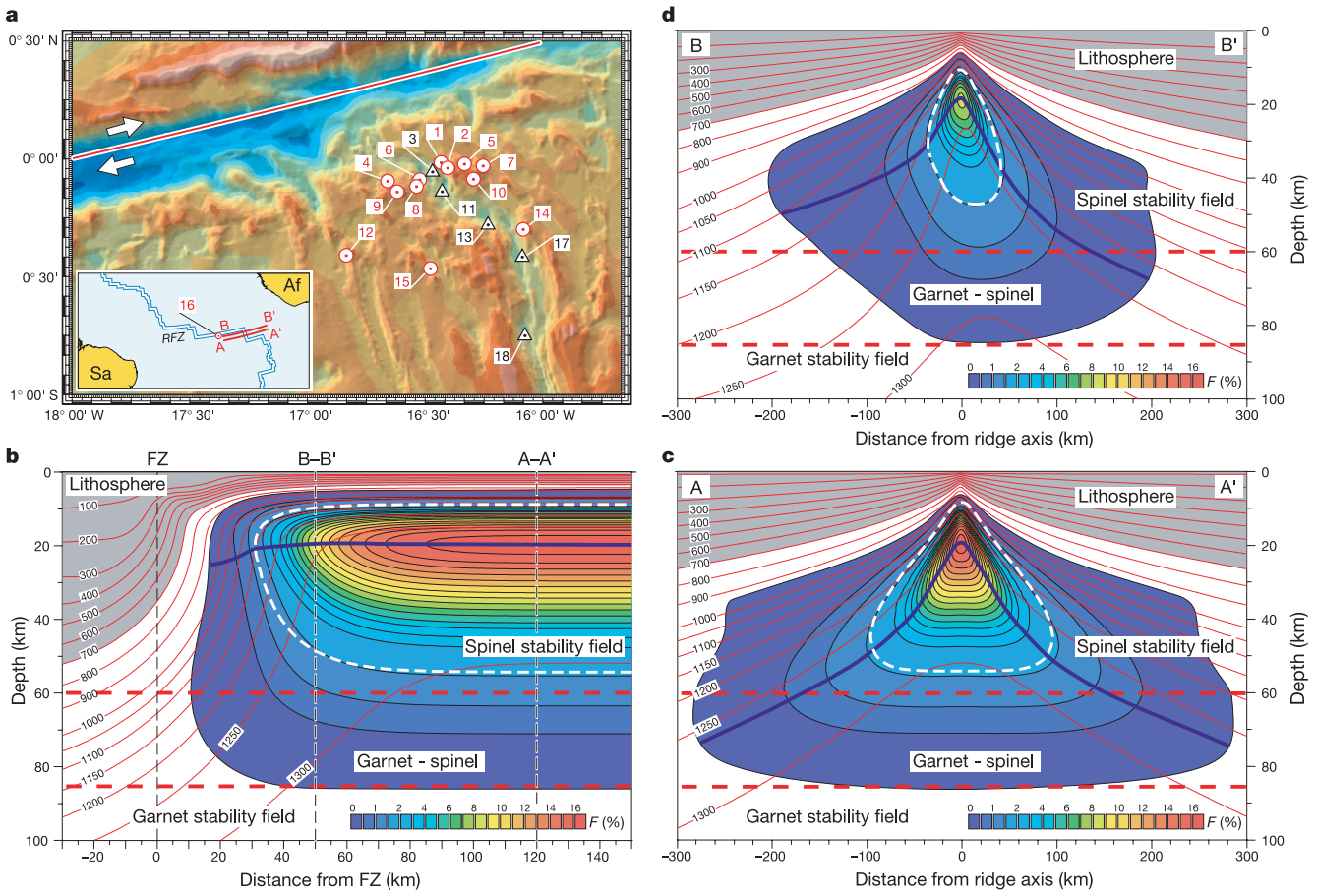


**Figure 3** Multibeam topography of the eastern Romanche ridge–transform intersection and predicted melt production beneath the ERRS. **a**, Shaded relief image based on multibeam data. Depth ranges from 7,800 m (dark blue) to 1,000 m (light grey). Spreading direction and small circle path (thick red solid line) have been computed using the Africa–South America eulerian vector of the NUVEL-1A model[29]. Sample locations (Supplementary Table) are indicated by red circles (this work) and black triangles. Numbers refer to position of samples in the Supplementary Table. Inset: RFZ, Romanche fracture zone; A–A′ and B–B′, location of sections shown in **c** and **d**. **b**, Fraction of melt (*F*, colour coded) generated along the ERRS axis, including the effect of water on peridotite solidus. The shape of the melting region is affected by mantle flow regimes (passive or active). We neglected the effects of viscosity heterogeneity and buoyancy in our numerical experiments. The thick white dashed line marks the region of dry melting. The thick dark purple solid line marks the upper boundary of the region of melt production, that is, where the production rate is positive. Thick red dashed lines indicate boundaries between garnet and spinel stability fields. Mineral proportions in the transition zone between 85 and 60 km are assumed to vary linearly from pure garnet peridotite to pure spinel peridotite. Isotherms (°C) are indicated by thin red lines. **c**, **d**, Across-axis sections showing fraction of melt generated at the ERRS centre (120 km; **c**) and in the proximity (50 km) of the ridge–transform intersection (**d**).

offset, a half spreading rate of 16 mm $yr^{-1}$ and that the bases of rigid plates were determined by the 700 °C isotherm (Fig. 2). The ridge segment intersecting the transform was assumed to be 512 km long, longer than the real ERRS, in order to evaluate how far the transform effect extends along axis, avoiding numerical edge effects. Assuming a $H_2O$ content of ~175 p.p.m. in the upper mantle[15] the peridotite solidus is lowered, causing partial melting in a subridge mantle region that is wider and deeper than it would be if the mantle were dry[16,17]. We modelled melt generation, including the effect of $H_2O$ on the peridotite solidus, using a modified parameterization of experimental data from ref. 18. Batch and near-fractional melting are assumed, and simulated by mapping the melting interval from the batch melting experiments; water is treated as an incompatible component with a bulk distribution coefficient $D_{H_2O}$ that varies with pressure[15] (see Supplementary Discussion).

Our numerical results (Fig. 3) show a strong decrease of 'crustal production' as the ridge approaches the transform, and no melting at all in a 20–40-km-wide strip close to the fracture zone (Fig. 3b), in agreement with the observation that the basaltic crust is nearly absent in that strip[13]. A cross-ridge subtriangular melting region, ~600 km wide at its base, is predicted beneath the centre of the segment, where the maximum degree of melting is 16.5% (Fig. 3c).

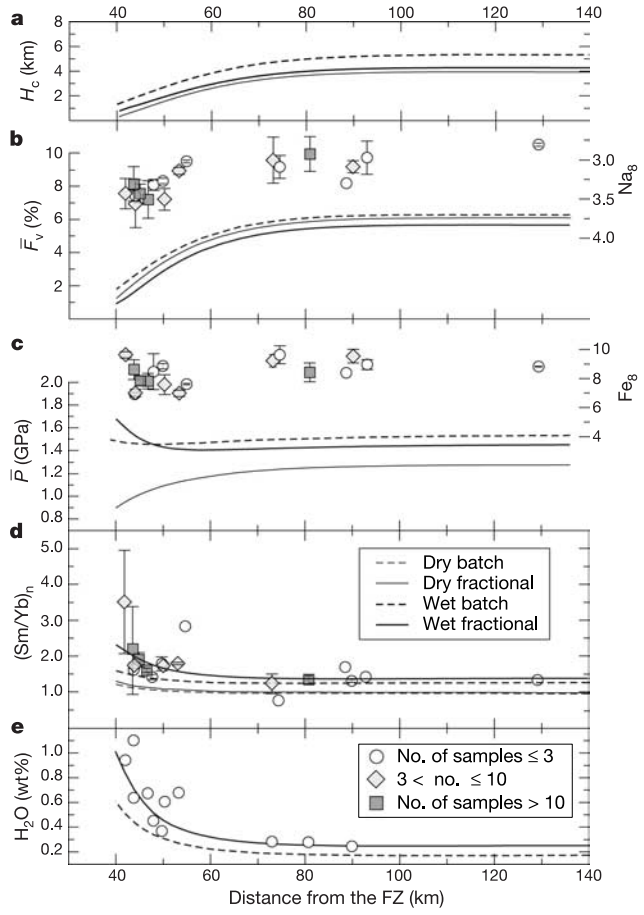


**Figure 4** Relationships between melt parameters predicted for MOR melting regimes and values obtained from the basalts sampled along the ERRS axis (Supplementary Table). **a**, Crustal thickness, $H_c$. **b**, Average degree of melting ($\bar{F}_V$, lines, left axis) and $Na_8$ (data points, right axis). **c**, Mean pressure of melting ($\bar{P}$, lines, left axis) and $Fe_8$ (data points, right axis). **d**, Chondrite-normalized[30] Sm/Yb ratio, $(Sm/Yb)_n$. The increasing influence of garnet as the ridge–transform intersection is approached is reflected by the increase of $(Sm/Yb)_n$ relative to the source. **e**, Models of water content in the aggregated melt and observed $H_2O$ concentrations in basaltic glasses. Error bars, ±1 s.d.

The melting region becomes smaller and asymmetric moving towards the ridge–transform intersection, with the maximum degree of melting decreasing rapidly (to ~8% at 50 km from the ridge–transform intersection), and the initial depth of melting varying greatly across axis (Fig. 3d).

Water addition deepens the onset of melting to 85 km beneath the centre of the segment, too cold for the anhydrous solidus to encounter garnet peridotite. Thus, water addition allows a significant melt fraction to be generated in the presence of residual garnet (Fig. 3c). In the proximity of the ridge–transform intersection, the partially molten region is mostly due to hydrous melting. The numerical model predicts that basalts sampled close to the Romanche fracture zone are generated exclusively in the subridge 'wet melting' mantle interval, that is, between ~80 and 60 km depth, within the region of stability of garnet. We would thus expect a significant 'garnet signature' in the chemical composition of our basalts, because they are undiluted by melts produced in the 'dry melting interval', above ~60 km depth within the spinel stability field.

REE partition coefficients during melting are different across the 80–60-km-deep boundary between garnet stability below, and spinel stability above: the heavy REEs are compatible with garnet but not with spinel. Thus, melting in the garnet stability field produces liquids depleted of heavy REEs relative to light REEs, and with chondrite-normalized Sm/Yb ratios, $(Sm/Yb)_n$, of well over one[19–21] and increasing with the proportion of melt generated in the garnet stability field. The deeper the level where the ascending mantle stops melting, the higher the proportion of melt generated in the presence of garnet[22].

The concentration of highly incompatible elements in the aggregated liquid should be inversely proportional to the mean degree of melting. Therefore, incompatible elements should be increasingly enriched moving along axis towards the ridge–transform intersection. We calculated crustal thickness, mean pressure of melting, mean degree of melting, and mean composition of the aggregate melt, at any location along axis from the centre towards the tip of the ERRS, for each of the following melting models: wet and dry; batch; near-fractional; and pure-fractional. Mantle mineral assemblages for garnet, spinel and plagioclase peridotite are those of ref. 23; REE source composition and distribution coefficients are from ref. 24.

Basalt $Na_8$, $(Sm/Yb)_n$ and $H_2O$ contents increase along axis towards the ridge–transform intersection, as predicted by the numerical model (Fig. 4). Note that when hydrous melting is included, the selected melting regime (batch, pure- or near-fractional) affects melting parameter predictions, owing to the pressure release melt parameterization adopted. The observed along-axis average patterns of melting parameter chemical indicators, such as $Na_8$, $Fe_8$ and REE concentrations (Fig. 4), suggest that a pure-fractional or near-fractional melting model with a very low residual porosity (<0.5%) fits the data best.

We conclude that the $H_2O$ content of the oceanic basaltic crust peaks not only close to hotspots, but also at 'cold spots' along MORs. However, whereas hotspot $H_2O$ maxima are caused by high degrees of melting of their $H_2O$-rich mantle plume sources, the $H_2O$ enrichment of 'cold spots' is due to low degrees of melting occurring mostly within the 'wet melting' depth interval below the ridge, largely within the garnet stability field, with minor dilution from shallower 'dry' melts. Our results are consistent with the ubiquitous presence in the deeper part of the subridge melting column of volatiles and enriched components that are tapped preferentially during incipient 'wet' melting, but which are normally diluted by more abundant 'dry' melts generated in the shallower part of the melting column.

Extrapolating from these results, we expect relatively high $H_2O$ content in basaltic crust generated at other 'thermal minima' along the MOR system, as at the Australian/Antarctic discordance[25] and at the Gakkel ridge[26]. □

## Methods

### Major elements

These were determined using a JEOL JXA 8600 microprobe at IGG-CNR, in Florence. The acceleration voltage was 15 kV, the sample current was 10 nA. The counting times were 40 s for Na and Cl and 10 s for all other elements; the spot size was 10 μm.

### $H_2O$

$H_2O$ content was determined by secondary ion mass spectrometry (SIMS) with a Cameca IMS 4f ion microprobe (at IGG-CNR in Pavia), following a procedure that involves 'energy filtered' secondary ions[27] (emission energies in the range 75–125 eV). Under these experimental conditions, the H background, measured on a sample of quartz, is typically 0.009 wt% $H_2O$. The values for $H_2O$ in the Supplementary Table are the average of three measurements. The accuracy of analysis is estimated to be 10% relative.

### REE

REE concentrations were determined with the Pavia ion microprobe. An optimized energy filtering technique was applied to remove complex molecular interferences in the secondary ion mass spectrum. Light-REE-rich basalts were analysed applying a deconvolution filter to the secondary-ion REE mass spectrum in order to reduce residual oxide interferences (that is, BaO on Eu, CeO and NdO on Gd, GdO on Yb, and EuO on Er). Precision of the measurement is of the order of 10% relative, for REE concentrations in the range 0.1–0.7 p.p.m. Below 0.1 p.p.m., precision is mainly limited by (poissonian) counting statistics and falls to ~30% relative. Accuracy is of the same order of precision. The experimental conditions involved a 9.5 nA, $^{16}O^-$ primary ion beam accelerated through −12.5 kV and focused into a spot 10–15 μm in diameter, and energy-filtered (75–125 eV) positive secondary ions detected under an ion image field of 25 μm.

Received 18 June; accepted 30 November 2004; doi:10.1038/nature03264.


1. Danyushevsky, L. V. The effect of small amounts of $H_2O$ on crystallisation of mid-ocean ridge and backarc basin magmas. *J. Volcanol. Geotherm. Res.* **110,** 265–280 (2001).
2. Michael, P. J. The concentration, behavior and storage of $H_2O$ in the suboceanic upper mantle — Implications for mantle metasomatism. *Geochim. Cosmochim. Acta* **52,** 555–566 (1988).
3. Nichols, A. R. L., Carroll, M. R. & Hoskuldsson, A. Is the Iceland hot spot also wet? Evidence from the water contents of undegassed submarine and subglacial pillow basalts. *Earth Planet. Sci. Lett.* **202,** 77–87 (2002).
4. Asimow, P. D., Dixon, J. E. & Langmuir, C. H. A hydrous melting and fractionation model for mid-ocean ridge basalts: Application to the Mid-Atlantic Ridge near the Azores. *Geochem. Geophys. Geosyst.* **5,** Q01E16, doi:10.1029/2003GC000568 (2004).
5. Dixon, J. E. & Clague, D. A. Volatiles in basaltic glasses from Loihi Seamount, Hawaii; evidence for a relatively dry plume component. *J. Petrol.* **42,** 627–654 (2001).
6. Dixon, J. E. & Stolper, E. M. An experimental study of water and carbon dioxide solubilities in mid-ocean ridge basaltic liquids. 2. Applications to degassing. *J. Petrol.* **36,** 1633–1646 (1995).
7. Klein, E. M. & Langmuir, C. H. Global correlations of ocean ridge basalt chemistry with axial depth and crustal thickness. *J. Geophys. Res.* **92,** 8089–8115 (1987).
8. Taylor, B. & Martinez, F. Back-arc basin basalt systematics. *Earth Planet. Sci. Lett.* **210,** 481–497 (2003).
9. Schilling, J. G. Azores mantle blob: The rare-earth evidence. *Earth Planet. Sci. Lett.* **24,** 103–105 (1975).
10. Bonatti, E. Not so hot "hot spots" in the oceanic mantle. *Science* **250,** 107–111 (1990).
11. Bonatti, E., Seyler, M. & Sushevskaya, N. A cold suboceanic mantle belt at the Earth's equator. *Science* **261,** 315–320 (1993).
12. Schilling, J. G. *et al.* Thermal structure of the mantle beneath the equatorial mid-Atlantic ridge—Inferences from the spatial variation of dredged basalt glass compositions. *J. Geophys. Res.* **100,** 10057–10076 (1995).
13. Bonatti, E. *et al.* Steady-state creation of crust-free lithosphere at cold spots in mid-ocean ridges. *Geology* **29,** 979–982 (2001).
14. Fox, P. J. & Gallo, D. The tectonics of ridge transform intersections. *Tectonophysics* **104,** 204–242 (1984).
15. Hirth, G. & Kohlstedt, D. L. Water in the oceanic upper mantle: Implications for rheology, melt extraction and the evolution of the lithosphere. *Earth Planet. Sci. Lett.* **144,** 93–108 (1996).
16. Braun, M. G., Hirth, G. & Parmentier, E. M. The effect of deep damp melting on mantle flow and melt generation beneath mid-ocean ridges. *Earth Planet. Sci. Lett.* **176,** 339–356 (2000).
17. Asimow, P. D. & Langmuir, C. H. The importance of water to oceanic mantle melting regimes. *Nature* **421,** 815–820 (2003).
18. Katz, R. F., Spiegelman, M. & Langmuir, C. H. A new parameterization of hydrous mantle melting. *Geochem. Geophys. Geosyst.* **4,** 1073, doi:10.1029/2002GC000433 (2003).
19. Gast, P. Trace element fractionations and the origin of tholeiitic and alkaline magma types. *Geochim. Cosmochim. Acta* **32,** 1057–1086 (1968).
20. Shen, Y. & Forsyth, D. W. Geochemical constraints on initial and final depths of melting beneath mid-ocean ridges. *J. Geophys. Res.* **100,** 2211–2237 (1995).
21. Hellebrand, E., Snow, J. E., Dick, H. J. B. & Hofmann, A. W. Coupled major and trace elements as indicators of the extent of melting in mid-ocean-ridge peridotites. *Nature* **410,** 677–681 (2001).
22. Ellam, R. M. Lithospheric thickness as a control on basalt geochemistry. *Geology* **20,** 153–156 (1992).
23. McKenzie, D. & O'Nions, R. K. Partial melt distributions from inversion of rare earth element concentrations. *J. Petrol.* **32,** 1021–1091 (1991).
24. Hellebrand, E., Snow, J. E., Hoppe, P. & Hofmann, A. W. Garnet-field melting and late-stage refertilization in "residual" abyssal peridotites from the central Indian ridge. *J. Petrol.* **43,** 2305–2338 (2002).
25. Christie, D. M., West, B. P., Pyle, D. G. & Hanan, B. B. Chaotic topography, mantle flow and mantle migration in the Australian-Antarctic discordance. *Nature* **394,** 637–644 (1998).
26. Michael, P. J. *et al.* Magmatic and amagmatic seafloor generation at the ultraslow-spreading Gakkel ridge, Arctic Ocean. *Nature* **423,** 956–961 (2003).
27. Ottolini, L., Bottazzi, P., Zanetti, A. & Vannucci, R. Determination of hydrogen in silicates by secondary ion mass spectrometry. *Analyst* **120,** 1309–1314 (1995).
28. Phipps Morgan, J. & Forsyth, D. W. Three-dimensional flow and temperature perturbations due to a transform offset: Effects on oceanic crustal and upper mantle structure. *J. Geophys. Res.* **93,** 2955–2966 (1988).
29. DeMets, C., Gordon, R. G., Argus, D. F. & Stein, S. Effect of recent revisions to the geomagnetic reversal time scale on estimates of current plate motions. *Geophys. Res. Lett.* **21,** 2191–2194 (1994).
30. Anders, E. & Grevesse, N. Abundances of the elements: Meteoritic and solar. *Geochim. Cosmochim. Acta* **53,** 197–214 (1989).


**Supplementary Information** accompanies the paper on **www.nature.com/nature**.

**Acknowledgements** We thank D. Brunelli for comments, and D. W. Forsyth for providing programs for temperature calculations. This work was supported by the Italian Consiglio Nazionale Ricerche, the US National Science Foundation and the EUROMARGINS programme.

**Competing interests statement** The authors declare that they have no competing financial interests.

**Correspondence** and requests for materials should be addressed to E.B. (enrico.bonatti@bo.ismar.cnr.it).

# Kin selection and cooperative courtship in wild turkeys

**Alan H. Krakauer**

*Department of Integrative Biology and Museum of Vertebrate Zoology, University of California, Berkeley, California 94720-3160, USA*

**In the few species of birds in which males form display partnerships to attract females, one male secures most or all of the copulations[1,2]. This leads to the question of why subordinate males help in the absence of observable reproductive benefits. Hamilton's concept of kin selection[3], whereby individuals can benefit indirectly by helping a relative, was a crucial breakthrough for understanding apparently altruistic systems. However in the only direct test of kin selection in coordinated display partnerships, partners were unrelated[1], discounting kin selection as an explanation for the evolution of cooperation. Here I show, using genetic measures of relatedness and reproductive success, that kin selection can explain the evolution of cooperative courtship in wild turkeys. Subordinate (helper) males do not themselves reproduce, but their indirect fitness as calculated by Hamilton's rule[3,4] more than offsets the cost of helping. This result confirms a textbook example of kin selection[2] that until now has been controversial[5] and also extends recent findings[6–8] of male relatedness on avian leks by quantifying the kin-selected benefits gained by non-reproducing males.**

The observation that cooperation in birds typically occurs between relatives[9] is superficial support for the idea that kin selection is a general explanation for avian helping behaviour. However, most examples of helping or cooperative breeding involve offspring retained in intergenerational family groups[9,10] in which it is difficult to separate the indirect fitness benefits due to kin selection from benefits due to direct fitness[11], even when the dynamics of helping behaviour qualitatively fits the predictions of Hamilton's rule[12]. Species with aggregated male displays are therefore valuable for studying kin selection because it is possible to isolate the role of indirect fitness in the absence of direct benefits stemming from delayed dispersal. Surprisingly, the role of kin selection on leks has only recently been proposed[13], and kin associations of displaying males have now been demonstrated for several species including grouse[6], peafowl[7] and manakins[8]. This